Geochemistry Geophysics Geosystems G3

Article
Volume 13, Number 5
2 May 2012
Q05002, doi:10.1029/2012GC004041
ISSN: 1525-2027

Published by AGU and the Geochemical Society

Controls of bathymetric relief on hydrothermal fluid flow at mid-ocean ridges

Nasser Bani-Hassan, Karthik Iyer, and Lars H. Rüpke
GEOMAR, Helmholtz Centre for Ocean Research Kiel, Wischhofstr. 1-3, D-24148 Kiel, Germany (nbanihassan@geomar.de)

Andrea Borgia
Lawrence Berkeley National Laboratory, 1 Cyclotron Road, Berkeley, California 24790, USA

EDRA, via di Fioranello 31, I-00134 Rome, Italy

Department of Earth and Environmental Sciences, Open University, Walton Hall, Milton Keynes MK7 6AA, UK

[1] We present quantitative modeling results for the effects of surface relief on hydrothermal convection at ocean-spreading centers investigating how vent site locations and subsurface flow patterns are affected by bathymetry induced sub-seafloor pressure variations. The model is based on a 2-D FEM solver for fluid flow in porous media and is used to simulate hydrothermal convection systematically in 375 synthetic studies. The results of these studies show that bathymetric relief has a profound effect on hydrothermal flow: bathymetric highs induce subsurface pressure variations that can deviate upwelling zones and favor venting at structural highs. The deviation angle from vertical upwelling can be expressed by a single linear dependence relating deviation angle to bathymetric slope and depth of the heat source. These findings are confirmed in two case studies for the East Pacific Rise at 9°30′N and Lucky Strike hydrothermal fields. In both cases, it is possible to predict the observed vent field locations only if bathymetry is taken into account. Our results thereby show that bathymetric relief should be considered in simulations of submarine hydrothermal systems and plays a key role especially in focusing venting of across axis hydrothermal flow onto the ridge axis of fast spreading ridges.

Components: 9800 words, 9 figures, 1 table.

Keywords: Lucky Strike; bathymetry; hydrothermal convection; vent location.

Index Terms: 0545 Computational Geophysics: Modeling (1952, 4255, 4316); 3017 Marine Geology and Geophysics: Hydrothermal systems (0450, 1034, 3616, 4832, 8135, 8424); 3021 Marine Geology and Geophysics: Marine hydrogeology.

Received 11 January 2012; **Revised** 30 March 2012; **Accepted** 31 March 2012; **Published** 2 May 2012.

Bani-Hassan, N., K. Iyer, L. H. Rüpke, and A. Borgia (2012), Controls of bathymetric relief on hydrothermal fluid flow at mid-ocean ridges, *Geochem. Geophys. Geosyst.*, *13*, Q05002, doi:10.1029/2012GC004041.

1. Introduction

[2] Hydrothermal systems are ubiquitous geological features in areas where heat flow is high and fluids can readily circulate through a permeable matrix. In fact, hydrothermal flow through the Earth's crust has frequently a first order control on major geological processes active on the seafloor. For example, hydrothermal venting is closely linked to the genesis of oceanic crust. Seawater enters the young ocean floor along fractures and cracks to reach and react with a hot magmatic intrusion forming mineral-rich buoyant hydrothermal brine. Regardless of setting, a challenge to submarine hydrothermal research is that the physicochemical processes that control them occur deep inside the Earth's crust and are largely inaccessible to direct sampling. Nevertheless, much has been learned from fluid geochemistry, petrological and geochemical studies, geophysical imaging, thermodynamics, and numerical simulations [e.g., *Allen and Seyfried*, 2003; *Bach et al.*, 2004; *Charlou et al.*, 1996, 2002; *Cherkaoui et al.*, 2003; *Coumou et al.*, 2009a; *Iyer et al.*, 2010, 2008; *Murton et al.*, 1994; *Von Damm*, 1990; *Wilcock*, 1998]. The venting of these hydrothermal fluids back into the ocean is of major importance as it is associated with enhanced cooling of the ocean floor, formation of deep-sea ore deposits, and unique ecosystems that exist around vent sites in extreme environmental conditions [*Boetius*, 2005; *Cathles et al.*, 1997; *Fouquet et al.*, 1995; *Haymon et al.*, 1989; *Kelley et al.*, 2005; *Lister*, 1980; *Marques et al.*, 2007; *Tufar et al.*, 1986].

[3] Mid-ocean ridges with their intense magmatic and hydrothermal activities are good examples where we can study the effects of bathymetry on submarine hydrothermal flow. At both, fast and slow spreading ridges, formation of new oceanic crust is controlled by a combination of magmatic, tectonic and hydrothermal processes. Fast spreading ridges, like the East Pacific Rise, are likely to be in steady state and have a stable melt lens beneath the ridge axis [*Baran et al.*, 2005; *Morgan and Chen*, 1993]. Their topography is characterized by an axial high on the order of hundred meters in height whereas the lateral extension may reach several kilometers [*Carbotte and Macdonald*, 1994] and hydrothermal venting appears to be exclusively located directly on-axis [*Baker and German*, 2004]. Slow-spreading ridges are more complex and undergo shifting periods of magmatic and tectonic phases [*Escartín et al.*, 2008]. They are most likely not in steady state and a stable melt lens has so far only been imaged beneath the magmatically active Lucky Strike segment on the Mid-Atlantic Ridge [*Singh et al.*, 2006]. The bathymetry of slow-spreading ridges show mostly wide, deep median valleys with highly variable relief in excess of 1000 m that can be up to 10 km in width [e.g., *Coakley and Cochran*, 1998; *Dick et al.*, 2003; *Kleinrock et al.*, 1997; *Searle et al.*, 1998; *Smith and Cann*, 1992; *Tolstoy et al.*, 2001]. Vent fields have been reported both on-axis (e.g., 5°S [*Koschinsky et al.*, 2008], Lucky Strike [*Dusunur et al.*, 2009]) as well as off-axis (e.g., Logatchev [*Schmidt et al.*, 2007], TAG [*deMartin et al.*, 2007]). Direct observations indicate that magmatic hydrothermal systems at mid-ocean ridges often vent at bathymetric highs. For example, the Lucky Strike vent-field is located on the ridge axis above the Axial Magma Chamber (AMC) on a central volcanic cone. At fast spreading ridges, the situation is somewhat simpler as most hydrothermal venting occurs on-axis on top of the axial high [*Baker and German*, 2004]. At the East Pacific Rise (9°40′N, 104°17′W), for example, a band of seismicity above the magma chamber illustrates that hydrothermal activity is aligned along the ridge axis [*Tolstoy et al.*, 2008].

[4] At both fast- and slow-spreading ridges, the locations of hydrothermal venting are likely to be controlled by a multitude of parameters including permeability structure, heat source location and crustal accretion mode. Previous studies have addressed submarine hydrothermal flow using numerical models of different complexities. Single phase studies were carried out by numerous researchers [*Coumou et al.*, 2008, 2009b; *Fontaine and Wilcock*, 2007; *Theissen-Krah et al.*, 2011; *Wilcock*, 1998]. More sophisticated multiphase studies on convection patterns were recently performed as well [*Coumou et al.*, 2009a]. However, the effect of bathymetric relief was largely neglected in these studies. The impact of topography on subaerial systems is well known [*Ingebritsen et al.*, 2006]: groundwater flow is directed from relative highs in the water table to relative lows so that venting is likely to occur in structural lows and recharge occurs in structural highs. The opposite occurs in submarine hydrothermal systems where venting occurs in bathymetric highs. The physics of the focusing effect of bathymetric relief on hydrothermal venting into the highs can be explained by closer inspection of the temperature and pressure fields of submarine hydrothermal systems and has been already described by previous work [*Ingebritsen et al.*, 2006]. Pressure at the seafloor is controlled by water depth, while the pressure inside the crust is additionally influenced by the density of the pore fluids. Steady state conductive geotherms mimic the bathymetric relief and are

Table 1. List of Model Parameters

Parameter	Symbol	Value (Synthetics)	Value (Case Studies)	Unit
Density of fluid	ρ_f	Based on PROST	Based on PROST	kg m^{-3}
Dynamic viscosity of fluid	μ_f	Based on PROST	Based on PROST	Pa s
Specific heat capacity of fluid	c_{pf}	Based on PROST	Based on PROST	J kg^{-1} K^{-1}
Pressure	P	Calculated	Calculated	Pa
Temperature	T	Calculated	Calculated	°C
Darcy velocity	$\vec{u}$	Calculated	Calculated	m s^{-1}
Density of matrix	ρ_m	2700	2750	kg m^{-3}
Specific heat capacity of matrix	c_{pm}	880	880	J kg^{-1} K^{-1}
Porosity of matrix (synthetics)	φ	0.1	0.01	
Permeability of matrix	k	5×10^{-15}	Variable	m^2
Thermal conductivity	λ	2	2.25	W m^{-1} K^{-1}
Thermal expansion coefficient	α	Calculated	Calculated	
Compressibility factor	β	Calculated	Calculated	
Gravitational acceleration	g	9.81	9.81	m s^{-2}
Time	t			s

consequently deflected upwards below bathymetric highs. As fluid densities are strongly temperature dependent, this thermal structure controls the pressure field and results in relative pressure lows below structural highs. As a consequence, a lateral force will be exerted driving convection from the high toward the low pressure area (found beneath the bathymetric high) and any thermal plume will be forced to ascend toward and vent at bathymetric highs.

[5] This effect has, to some extent, been addressed by earlier studies [e.g., *Fisher et al.*, 1990; *Hartline and Lister*, 1981; *Lowell*, 1980]. *Fisher et al.* [1990] studied the influence of topography on the southern flank of the Costa Rican Rift and found that subcritical convection in the study area results in wide zones of fluid recharge occurring in the troughs accompanied by narrow discharge zones at the ridges. A similar result was also obtained by *Fisher et al.* [1994] who found that basement relief and differential sediment thickness play a greater role than bathymetry in enhancing passive, off-axis convection. More recently, *Kawada et al.* [2011] studied the influence of seamount aspect ratio and heat flow on fluid flow patterns within and around the seamount. They established that seamounts with high aspect ratio contain multiple convection cells irrespective of the crustal heat flow. On the other hand, small seamounts can act as a discharge zone when heat flow is low and act as a recharge zone if heat flow is high. However, a systematic study on bathymetry-driven fluid flow is still missing. Here we present a 2-D single phase model that is especially tailored to address this topic. In addition to a number of synthetic studies, we use observations from sites across the East Pacific Rise (9°30′N) and the Lucky Strike vent-fields as real-world counterparts in order to understand how bathymetry affects hydrothermal convection patterns.

2. Hydrothermal Convection Model

2.1. Governing Equations

[6] We have developed a hydrothermal flow model that is based on Darcy flow and resolves for pure water convection in porous media. The model formulation assumes that only one fluid phase is present at any spatial location and is, therefore, restricted to single phase flow of pure water during which phase separation does not occur. This simplification is justified as most mid-ocean spreading centers are located at water depths in excess of or at least close to the critical end-point of pure water (~220 bar).

[7] Equation (1) describes mass conservation in porous media, considering the fluid is compressible and porosity is constant

$$\phi \frac{\partial \rho_f}{\partial t} = -\nabla \cdot \left(\rho_f \vec{u} \right) \tag{1}$$

where $\vec{u}$ is the Darcy fluid velocity, ρ_f is fluid density, t is time and ϕ corresponds to matrix porosity (see Table 1 for complete list of variables and values). The velocity is defined by Darcy's Law

$$\vec{u} = -\frac{k}{\mu_f} \left(\nabla P - \rho_f \vec{g} \right) \tag{2}$$

Here k is the rock permeability, μ_f is the dynamic viscosity of the fluid, P is the fluid pressure and $\vec{g}$ is the gravitational acceleration. Substituting

equation (2) into equation (1) and by splitting density changes into their pressure and temperature parts, we obtain

$$\phi\rho_f\beta_f\frac{\partial P}{\partial t}=\nabla\cdot\left[\frac{k\rho_f}{\mu_f}\left(\nabla p-\rho_f\vec{g}\right)\right]+\phi\rho_f\alpha_f\frac{\partial T}{\partial t} \quad (3)$$

where α_f is fluid thermal expansion coefficient and β_f is fluid isothermal compressibility.

[8] The energy equation is described by

$$\left(\phi\rho_f c_{pf}+(1-\phi)\rho_m c_{pm}\right)\frac{\partial T}{\partial t}=-\rho_f c_{pf}\vec{u}\cdot\nabla T+\nabla\cdot(\lambda\nabla T) \quad (4)$$

where λ corresponds to effective thermal conductivity, T to temperature and c_p to specific heat capacity, which accounts for advective and conductive heat transport in addition to heat storage both in the fluid and the rock matrix. Subscript m and f denote matrix and fluid properties, respectively. Pressure-volume work and viscous dissipation are neglected in the energy equation [*Garg and Pritchett*, 1977]. Fluid properties of density, viscosity and specific heat capacity are treated as functions of pressure and temperature and are computed at every time step using the PROST library [*Bauer*, 1998] for the IAPWS-84 equation of state.

2.2. Numerical Implementation

[9] The governing equations are solved using a 2-D finite element approach in combination with an advection scheme. The solution is computed for every time step in sequential order: (1) thermal diffusion is resolved, (2) temperature is advected using the Darcy velocities, (3) fluid properties are evaluated, (4) new fluid pressure and porous flow velocities are then computed.

[10] The fluid pressure equation (equation (3)) is solved using finite elements. The weak form of this equation, derived by the Galerkin method, is

$$\begin{aligned}&\int_\Omega N'\bar{\phi}\ \bar{\beta}_f\bar{\rho}_f NP^n\ d\Omega+\int_\Omega\frac{\partial N'}{\partial x}\frac{\bar{k}\bar{\rho}_f}{\bar{\mu}_f}\Delta t\frac{\partial NP^n}{\partial x}\ d\Omega\\&+\int_\Omega\frac{\partial N'}{\partial y}\frac{\bar{k}\bar{\rho}_f}{\bar{\mu}_f}\Delta t\frac{\partial NP^n}{\partial y}\ d\Omega=-\int_\Omega\frac{\partial N'}{\partial y}\frac{\bar{k}}{\bar{\mu}_f}\Delta tg\bar{\rho}_f{}^2d\Omega\\&+\int_\Omega N'\bar{\alpha}_f\bar{\phi}\Delta t\bar{\rho}_f N\left(\frac{\Delta T}{\Delta t}\right)d\Omega+\int_\Omega N'\bar{\phi}\ \bar{\beta}_f\bar{\rho}_f NP^o d\Omega\\&+\oint_\Gamma N'\frac{\bar{k}\bar{\rho}_f}{\bar{\mu}_f}\Delta t\frac{\partial NP^n}{\partial x}d\Gamma+\oint_\Gamma N'\frac{\bar{k}\bar{\rho}_f}{\bar{\mu}_f}\Delta t\frac{\partial NP^n}{\partial y}d\Gamma\\&+\oint_\Gamma N'\frac{\bar{k}}{\bar{\mu}_f}\Delta tg\bar{\rho}_f{}^2d\Gamma\end{aligned} \quad (5)$$

where N is linear shape function for three-node triangle elements. Bars and primes denote averaged properties on an element and transposes, respectively. Superscripts n and o denote new and old time steps, respectively. Symbols Ω and Γ are computational domain and its boundaries, respectively. All fluid and rock properties are averaged over an element and all mass matrices are lumped. The pressure solution is obtained by implementing equation (5) into a modified version of the Matlab-based FEM solver MILAMIN by *Dabrowski et al.* [2008]. Taking derivatives of the pressure solution provides the updated Darcy velocities at element centers. These velocities are subsequently averaged onto nodes in order to use them with a node-based semi-Lagrangian advection scheme. Note that the fluid and matrix properties are calculated on the nodes and Darcy velocities are mapped on nodes by taking equal contributions of neighboring elements. This mapping could be avoided by the use of node-centered finite-volume techniques that use velocities at element centers [*Geiger et al.*, 2004]. We have experimented with both advection schemes and find that for single-phase calculations, the semi-Lagrangian approach does not have problems with mass conservation and allows for larger computational time steps. We have, therefore, used a semi-Lagrangian solver for the advective part of the energy equation (4) that uses the element shape functions for temperature interpolation. The diffusive part of equation (4) is again solved with the FEM scheme. This model was validated against the results of *Coumou et al.* [2006] and a previous version of the model was also benchmarked against *Cherkaoui and Wilcock* [1999] [*Iyer et al.*, 2010].

3. Synthetic Studies

[11] This section aims at constraining the effects of bathymetric relief on hydrothermal convection. Two sets of simulations are carried out. The first set explores the effect of a single bathymetric high on a single plume and the second set of simulations takes into account the effect of multiple bathymetric highs on multiple plume formation. Simulations with a flat seafloor are used as reference cases for both sets which are then used to discuss the effects of bathymetry. The synthetic studies with bathymetric relief are referred to as non-references cases. All simulations are run until a quasi-steady state is approached; i.e., the single high and multiple high simulations are run for 10,000 and 3000 years, respectively. The fluid and matrix parameters used in the simulations with bathymetric relief are the

same as those used in the corresponding reference case simulation. The matrix is homogeneous and its properties are kept constant throughout the run for all synthetic simulations. The values for matrix properties are listed in Table 1. The number of elements used in the simulations is approximately 8,300 elements per square kilometer.

3.1. Single Bathymetric High

3.1.1. Model Geometry and Setup

[12] The domain in the single bathymetric high simulations is 4600 m wide while the depth is varied between 1000 and 2000 m. The bathymetric high is triangular in shape and rises above the flat surface of the domain. The starting point of the bathymetric high is fixed at distance of 1450 m. The flat surface of the 2-D domain is kept at a constant pressure of 30 MPa simulating a seafloor depth of ~3 km to ensure that phase separation does not occur in experiments with the highest elevation of the peak. The surface rising above the flat part is kept at a pressure corresponding to its depth. Temperature in the model is initialized to 10°C and the model is heated at the bottom boundary by a Gaussian heat source located at distance of 1500 m. The maximum temperature of the heat source is 1000°C and the width of Gaussian function is 1/12 of the box size in the x-direction. The defined width of the Gaussian heat source ensures that only a single plume is formed in the simulations. The side-boundaries of the box are insulating and the sides and bottom boundaries of the box are impermeable. An upper boundary condition is applied to allow the fluid to vent freely where the plume reaches the surface and allow water at 10°C to enter the domain in recharge zones. This condition is applied by calculating the direction of fluid vectors at the upper boundary nodes.

3.1.2. Reference Simulation

[13] A single hydrothermal plume forms at the bottom heat source and ascends vertically to reach the surface right above the center of the heat source. Plume-splitting is observed initially at the bottom of model, but the single plume is rapidly established. The plume vents at the surface after 750 years of convection when the model depth is 1500 m and reaches steady state.

3.1.3. Non-reference Simulations

[14] The non-reference simulations are used to study the maximum deviation of the plume from its original vent location as observed in the reference simulation in the presence of a single bathymetric high. The dimensions of the high are defined by its wavelength (half-width of the high) as well as its amplitude (elevation of the summit with respect to the flat seafloor) which in turn controls how much the plume could deviate from its original vent location. The wavelength and amplitude of the high is systematically varied from 500 to 1500 m in 250 m increments and 100 to 500 m in 50 m increments, respectively. A single plume is initially formed and vents at the seafloor, right above the center of heat source as observed in the reference simulation. The plume migrates toward the summit of the bathymetric high with time and finally reaches a steady state. The time after which plume migration begins and the time required for migration to complete before a steady state is reached depends on the wavelength and amplitude of the prescribed bathymetric high. The results show that plume deviation and migration time of the plume is inversely dependent on the wavelength and directly dependent on the amplitude (Figure 1). An increase in wavelength results in an increase in the distance of the summit from the original plume location, thereby decreasing the control of bathymetry on convection whereas an increase in amplitude directly amplifies this effect. The plume can deviate toward the summit completely for relatively low wavelengths and high amplitudes. Conversely, if the wavelength and amplitude are relatively high and low, respectively, migration of the plume stops at some distance away from the summit. We find that the lateral deviation of the plume divided by its vertical extent, a value easily converted to the plume deviation angle relative to the vertical (θ), can be expressed as a linear function of bathymetric slope (amplitude/wavelength) (Figure 2a). In the following we will refer to this value as relative plume deviation (D = lateral plume deviation/vertical plume extent). The results show a further dependence on the depth of the heat source (Figure 2a), which is systematically varied between 1000 and 2000 m in 250 m increments. The deeper the heat source, the less pronounced is the impact of bathymetry on plume deviation. This can be explained by the diminishing relative pressure difference caused by the bathymetric high as depth is increased. We find that the heat source depth has a linear influence on the coefficients of the dependence between relative plume deviation and bathymetric slope so that a single general relationship between relative plume deviation,

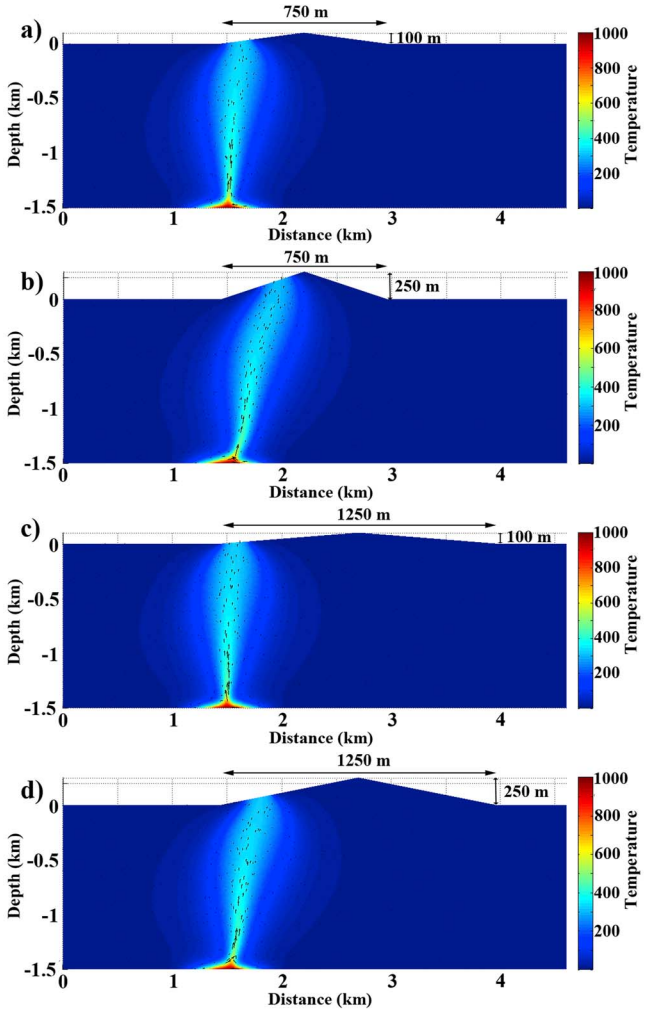

Figure 1. Simulations with a single plume and a single bathymetric high at steady state. Four examples are presented with the bathymetric high dimensions of (a) amplitude 100 m and wavelength 750 m, (b) amplitude 250 m and wavelength 750 m, (c) amplitude 100 m and wavelength 1250 m and (d) amplitude 250 m and wavelength 1250 m. The results show that the maximum deviation of the single plume from its origin is proportional to the amplitude and wavelength of the bathymetric high.

bathymetric slope and depth of heat source can be formulated

$$D\left(\frac{A}{W},z\right) = f(z)\frac{A}{W} + h(z)$$
$$f(z) = -5.65 \times 10^{-4} z + 2.178 \quad (6)$$
$$h(z) = -1.82 \times 10^{-4} z + 0.229$$
$$\theta = \tan^{-1}(D)$$

where A is the amplitude (m), W is the wavelength (m), and z is depth of the heat source (m). Figure 2b shows good agreement between the simulation results and the functional dependence described in equation (6). A linear least squares fit yields a slope of 0.986 and a regression coefficient of 0.983 showing that equation (6) can be used to approximate the effect of a single bathymetric feature on subsurface fluid flow if the location of the heat source is known.

3.2. Multiple Bathymetric Highs

3.2.1. Model Geometry and Setup

[15] The domain in the 2-D synthetic simulations with multiple bathymetric highs is 3.6 km wide and 1 km deep. The bathymetric relief, in the non-reference cases, is represented by a sinusoidal wave with varying amplitudes and wavelengths.

[16] The turning point of the sinusoidal surface in the simulated domain is overlain by 2.5 km of

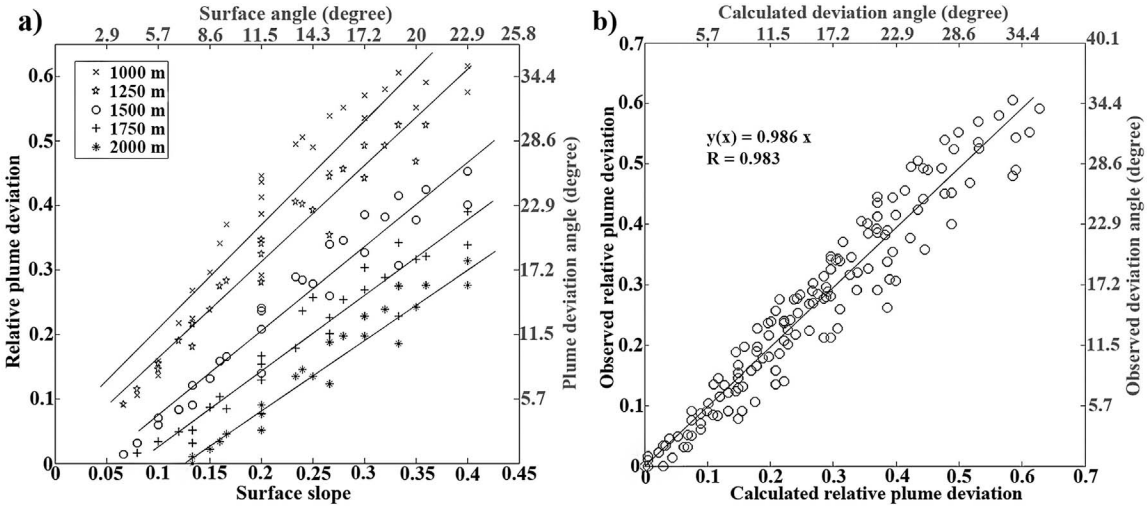

Figure 2. (a) Relative plume deviation (lateral plume deviation/vertical plume extent) as a function of surface slope for different model depths. The results suggest a linear relationship between plume deviation and surface slope. Model depth also influences this relationship while retaining the linear fit. (b) The observed relative plume deviation for a single plume for different amplitudes, wavelengths and model depths against the relative plume deviation derived from equation (6).

seawater and the temperature in the domain is initialized to 10°C. The domain is continuously heated at the bottom at a temperature of 1000°C mimicking the effect of a stable magmatic heat source. Similar to the single bathymetric high simulations, the side-boundaries of the box are insulating and the sides and bottom boundaries of the box are impermeable. The temperature upper boundary condition is also the same as that applied to the single bathymetric high simulations. The non-reference simulations are carried out for surface wavelengths of 3600, 1800, 900, 720, 600, 514, 450, 400, 360 and 300 m corresponding to between 2 and 11 bathymetric highs, respectively, while the amplitude varies between 20 m and 300 m, by 20 m increments for all the wavelengths.

3.2.2. Reference Simulation

[17] In the reference simulation, several plumes are initially formed at the base of the box where the temperature gradient and subsequently, the density and viscosity gradients in the fluid are highest. These plumes coalesce during their ascent to the surface to form fewer stable upwelling zones (Figure 3) and sometimes exhibit plume-splitting phenomena similar to that seen by *Coumou et al.* [2006]. For the given model setup, the simulation evolves toward a quasi steady state after ~1250 years of convection where eight plumes reach the surface at a fixed distance from each other. A number of smaller plumes are formed at the base of the domain but they are quickly assimilated in the larger, established plumes (Figure 3). The average distance between the plumes is ~514 m. The aspect ratio of a convection cell is defined as $A = D/2H$, where D is the distance between two adjacent plumes and H is the depth of the domain. The aspect ratio for the convection cells in the reference simulation is therefore 0.25, which is consistent with the results of simulations performed by *Coumou et al.* [2006].

3.2.3. Non-reference Simulations

[18] In these numerical experiments, the bathymetry is represented by a sinusoidal wave with varying amplitude and wavelength. A surface with periodic bathymetry and a constant temperature bottom boundary is selected in order to study the effect of multiple highs on multiple plumes while accounting for the interaction between different plumes.

[19] Figure 4 shows the results for selected example runs after 3000 years model run time. All left panel plots show the temperature field and all right panel plots show corresponding histograms of fluid venting as functions of bathymetric relief. Note that the depth of the surface is normalized to the amplitude of the bathymetric relief with the turning point of the surface slope taken as the zero value. A first order observation is that venting generally tends toward bathymetric highs in the presented simulations. Both wavelength and amplitude control how

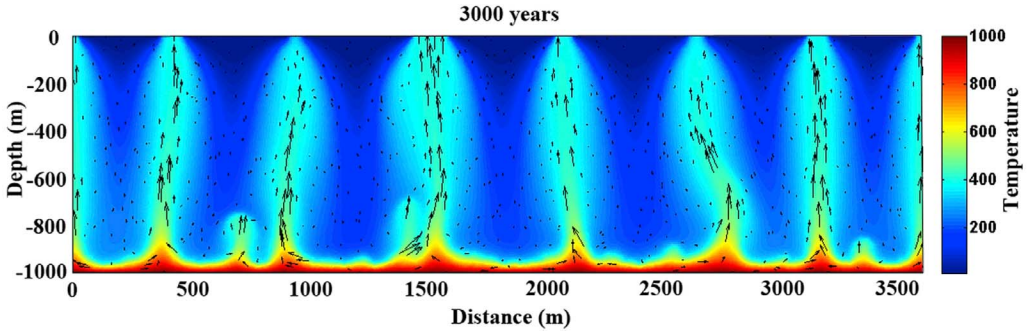

Figure 3. Temperature plot of the reference simulation with multiple plumes and constant temperature bottom heat source. The system approaches a quasi steady state at the end of simulation with eight plumes. The aspect ratio for the convection cells is 0.25 and the average distance between plumes is 514 m.

effectively venting is focused into bathymetric highs. Simulations in Figures 4a–4c illustrate the effects of relief wavelength for a fixed amplitude of 40 m. The tendency of venting at bathymetric highs increases as the wavelength decreases. Figures 4c and 4i show that venting occurs exclusively in the bathymetric highs when the number of bathymetric highs is comparable to or less than the number of plumes in the reference simulation. If the wavelength is increased, venting is more widely distributed over the surface (Figures 4a and 4g).

[20] The amplitude of bathymetric relief also has a strong effect: as amplitude increases, venting is progressively more focused into bathymetric highs. The bottom three simulations in Figure 4 demonstrate the effect of amplitude for a fixed wavelength of 1800 m. The results show that at low amplitude venting may occur at the flanks or even bathymetric lows (Figures 4d and 4j), but the plumes increasingly migrate toward bathymetric highs when the amplitude is increased (Figures 4e, 4f, 4k and 4l). In general, stronger deviations from vertical plume ascent toward bathymetric highs are found with increasing amplitude. Plumes may vent at flanks and lows during the initial stages of the simulations but are shifted toward the highs as the plumes evolve in time.

[21] The preceding section showed that both amplitude and wavelength control vent field location. To further explore the focusing of venting at bathymetric highs, the time-integrated mass fraction of vent fluids exiting within the upper half of bathymetric highs is plotted as a function of wavelength and amplitude in Figure 5a. The intersections of the gridlines are the locations of data points. The mass flux is integrated over time starting after 1000 years of convection when all the plumes have reached the surface until 3000 years of convection when the simulation is in a quasi steady state. The plot summarizes the characteristics of the relationships between amplitude and wavelength discussed above. If the wavelength is slightly larger or smaller than the plume spacing in the reference case (∼514 m), a bathymetric relief of only ∼40 m amplitude is sufficient to focus venting into bathymetric highs. If the wavelength is now increased, venting also occurs at flanks or even lows. This de-focusing effect of increasing wavelength can be compensated by increasing amplitude. There is, however, a limit to this: if amplitudes become very large for small wavelengths, venting again tends to occur at flanks as well which occurs when the size of the ascending plume head is larger than the width of the bathymetric high. This behavior suggests that the focusing effects of amplitude and wavelength can be summarized by a single parameter. Figure 5b shows that all values plotted in Figure 5a do collapse onto a bell-shaped curve if plotted against slope at the turning point of the sinusoidal relief. The curve shows maxima approximately between 30° and 60° where all the surface slopes steeper or gentler will result in lower focusing of plumes at the bathymetric highs. Therefore, the curve can be split into three regions: low-angle (<30°, zone 1), medium-angle (30°–60°, zone 2) and high-angle (>60°, zone 3) surfaces. As observed, maximum venting is achieved through the bathymetric highs where the surface angle lies in zone 2. This suggests that the probability of finding vent-sites at bathymetric highs is roughly proportional to seafloor slope. The simulations were also conducted using deeper and shallower domains. The results for these simulations do not significantly differ from those presented above and the maximum volume of venting at the highs still occurs at slopes between ∼30° and ∼60° similar to the previous simulations. The results obtained from section 3.1 combined

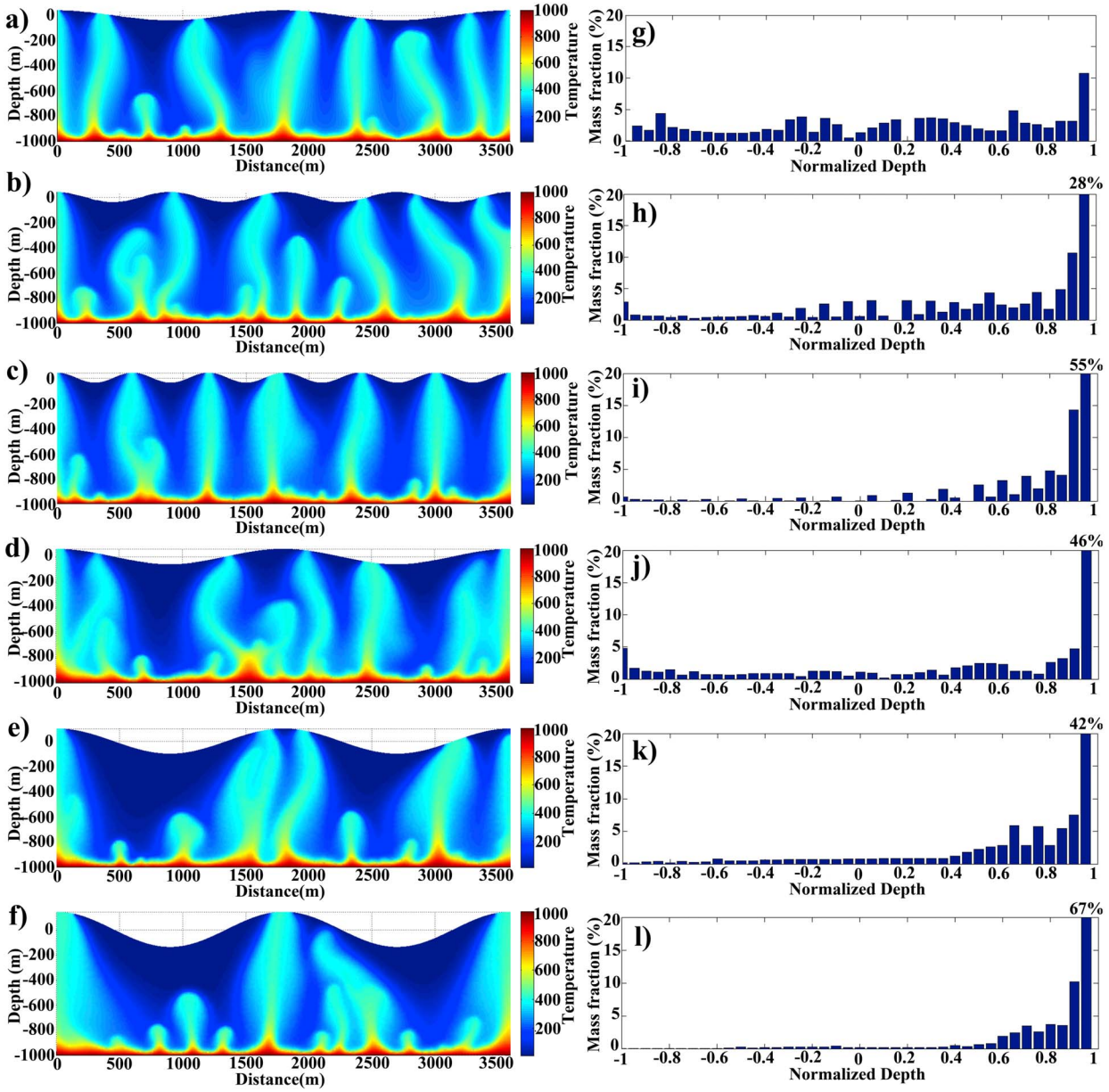

Figure 4. Simulation results showing the temperature fields for a selected number of variable bathymetric models. (a–c) The late stages of the models where the amplitude of the bathymetric relief is kept at 40 m with the wavelengths of 1800, 900 and 600 m, respectively. (d–f) The simulations where wavelength is kept constant at 1800 m with amplitudes of 60, 100 and 140 m. (g–l) Histograms of mass fraction of vent fluids versus surface bathymetry normalized to itself with the depth of the turning point as zero value.

with equation (6) allows for a qualitative assessment of the relation between the surface slope and amount of venting shown in Figure 5. A rigorous quantitative analysis is not possible due to the influence of plume interactions and due to the difference in slope variation used in the single and sinusoidal bathymetry simulations. Nevertheless, simulations with a surface slope of less than ~30° show less than optimal venting as the angle of deviation required for a plume farthest away from a bathymetric high to be present at that high is larger than the maximum angle of deviation calculated by equation (6) for the given parameters. Conversely, in simulations where the surface slope angle is greater than ~30°, the angle of deviation required for any plume to reach the closest high is less than the calculated maximum angle of deviation suggesting that complete migration to a high is possible. Simulations with a surface

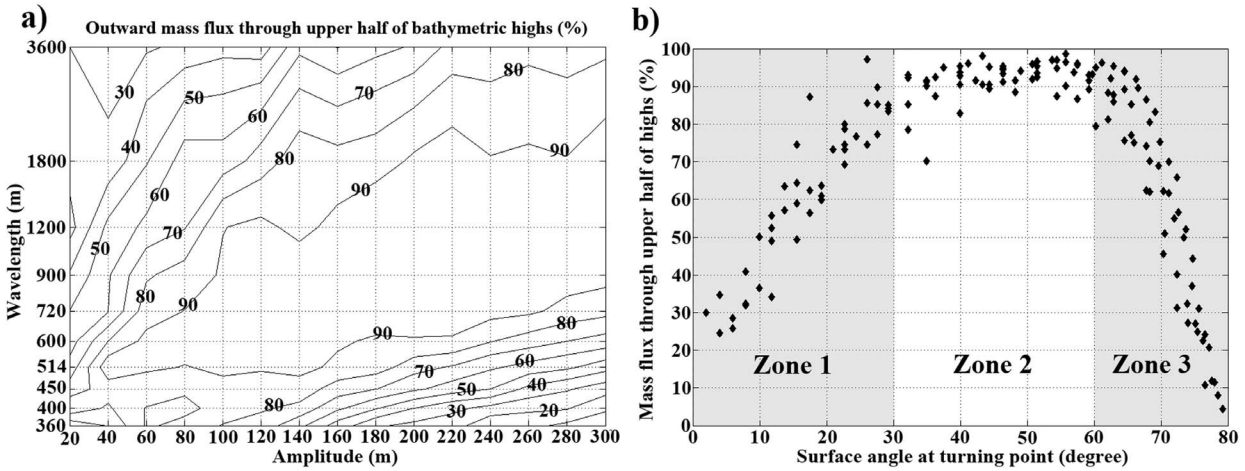

Figure 5. (a) Outward mass flux of vent fluid through the upper half of bathymetric highs (counted from the turning point) relative to total outward mass flux in a semi-logarithmic scale as a function of amplitude and wavelength of the sinusoidal surface relief. The gridline intersections are the location of the simulation results. (b) Outward mass flux of vent fluid through the upper half of bathymetric highs (counted from the turning point) relative to total outward mass flux for all 150 multiple-plume synthetic simulations as a function of the surface slope at the turning points. The plot can be differentiated into three zones: zone 1 (surface angle < 30°) where venting is not focused at bathymetric highs as the maximum deviation angle allowed for the plumes to reach a high calculated from the single bathymetric high simulation is less than the required deviation angle; zone 2 (30° < surface angle < 60°) where venting is focused at the bathymetric highs as the calculated maximum deviation angle for the generated plumes is larger than the required deviation angle and zone 3 (surface angle > 60°) where venting is observed at flanks and lows in addition to bathymetric highs as the plume head is larger than the width of bathymetric highs.

slope greater than ∼60° show reduced venting at highs as the width of the plume head exceeds the width of bathymetric relief.

[22] As a cautious note it should be added that these results are somewhat dependent on initial conditions. The presented simulations all assume an initially cold domain so that the initial pressure regime is not influenced by bathymetry. Only when a plume reaches a bathymetric feature, the pressure field is affected by bathymetric relief. Conversely, if an initial geothermal gradient is assumed, the initial pressure field is already affected by bathymetric relief. However, since we have largely restricted ourselves to the analysis of steady states, which are only weakly dependent on initial conditions, our results keep their generality.

4. Case Studies

[23] The preceding section has shown that bathymetric relief can have strong controls on vent site location. We will now use these insights to analyze how venting at the fast spreading EPR at 9°N and the slow-spreading Lucky Strike segment are influenced by bathymetric relief.

4.1. East Pacific Rise Vent Field (9°30′N)

4.1.1. Geological Setting

[24] The EPR is characterized as a fast spreading ridge with an average full spreading rate of 110–150 mm/yr [*Foulger*, 2010]. The bathymetry at 9°N at EPR shows relatively smooth relief with an axial high corresponding to the ridge axis [e.g., *Toomey et al.*, 1994; *Tolstoy et al.*, 2008]. A nearly continuous shallow melt lens was imaged at a depth of ∼1.5 km below the seafloor [*Detrick et al.*, 1987]. The melt lens is extremely narrow with a thickness of 10–50 m and width of ∼1 km [*Kent et al.*, 1993]. Seismic tomography suggests that a "slot" of hot partially molten crust exists below the ridge axis with a width of about ∼6 km [*Dunn et al.*, 2000]; the width of this hot zone widens in the mantle region to nearly 15 km. *Fisher* [2003] has argued that this special shape of hot crust can be explained by off-axis hydrothermal cooling, which is consistent with the ideas on pervasive hydrothermal circulation developed at the Oman ophiolite [*Nicolas et al.*, 2003]. However, if this pervasive off-axis (and across axis) hydrothermal flow does exist, it apparently does not result in off-axis venting; nevertheless, further off-axis surveys are essential to confirm

this. All currently known vent sites are located directly on axis [*Haymon et al.*, 1991] including the sites at 2570 m water depth at 9°30′N [http://www.interridge.org/irvents/content/epr-9-30n]. Here we test if hydrothermal fluids rising along off-axis margins of the hot central temperature anomaly are likely to be focused onto the ridge axis by bathymetric relief.

4.1.2. Model Setup

[25] The East Pacific Rise (9°30′N) vent site was modeled based on a depth converted map derived from studies by *Dunn et al.* [2000] and a topographic sketch by *Carbotte and Macdonald* [1994]. We modeled two scenarios: one with a flat top and one with the actual bathymetric relief. The temperature is set to 10°C in the matrix and the pressure is set to hydrostatic values initially. A hot slot (1000°C) is assumed to start from 1.6 km below the seafloor and extends up to depth of 8 km (bottom of model). The width of this high temperature increases rapidly to up to ~20 km at the bottom of modeling domain. Relatively smooth bathymetric variations of up to 400 m occur within the modeling domain. The maximum elevation of the seafloor is located just above the melt lens. The sides of model are insulated and the sides as well as the bottom of the model are impermeable. The surface pressure varies with topography where the highest point of the domain lies at a depth of 2.57 km below sea level. The matrix permeability structure at the East Pacific Rise and at fast spreading ridges in general is not well known and few studies give quantitative estimates. *Theissen-Krah et al.* [2011] provided estimates for the permeability structure above the melt lens and suggest that this permeability must decrease off-axis - potentially as a consequence of alteration and mineral precipitation reactions. We largely follow the permeability model of *Theissen-Krah et al.* [2011] and extend it by higher permeability values in the deeper near- to off-axis crust to allow for deep hydrothermal flow as discussed above. We achieve this by employing a permeability model, in which the surface permeability decreases exponentially with depth to the anomalously hot zone. For numerical convenience this is done by using a steady state diffusion temperature field and defining matrix permeability as a function of this initial temperature field. The computed permeability is kept fixed though and does not evolve by temperature variations during simulations. The surface permeability at the ridge axis is assumed to be $\sim 6 \times 10^{-15}$ m^2, which is consistent with the estimates of *Theissen-Krah et al.* [2011]. The resulting permeability field is scaled by a lateral exponential decrease in permeability from 2000 m away from the ridge axis. This results in the following permeability model

$$k = 6 \times 10^{-15} \times \exp\left(-3.2 \times 10^{-3} T\right) \quad (7)$$

$$k^* = k \times \exp\left(-7 \times 10^{-4} x\right) \quad (8)$$

where x is the absolute distance from 2000 m away from the ridge axis (m), k^* is the revised permeability which is used as a substitute for k in equations (2), (3) and (5), and T the initial steady state conductive temperature (°C). This permeability model is plotted in Figure 6 and is consistent with the observed melt lens depth and allows for pervasive off-axis hydrothermal flow. However, our static model setup is not suited for making estimates on permeability so that it remains our best guess on the actual permeability structure at EPR. Hopefully more data in combination with dynamical models will help to further constrain the deep permeability at ridges in the future.

[26] The matrix properties are listed in Table 1. The number of elements used in these simulations is 1000 per square kilometer. A further assumption is that porosity is constant and that both permeability and porosity do not change during the simulations.

4.1.3. Results

[27] The modeled temporal evolution of hydrothermal convection beneath the East Pacific Rise is shown in Figure 7 (the figure dimensions are restricted to 5 × 5 km to enhance the visibility of venting region). The simulations were run for 50,000 years when a quasi-steady state is attained. The left panel plots show the result with a flat seafloor, while the right panel plots the ones with the actual bathymetric relief. In the early phases of the simulations (Figures 7a and 7c), multiple plumes form above the central slot of hot crust. The plumes later merge and form a few major upwelling zones at the top of magma lens. In both settings, small convection cells develop directly on the top of hot crust, while deep large convection cells develop off-axis with upwellings along the margins of the magma chamber and recharge zones extending several kilometers off-axis (Figure 6). A striking feature of the simulation with a flat seafloor is that venting does not occur on-axis but at two, near-axis

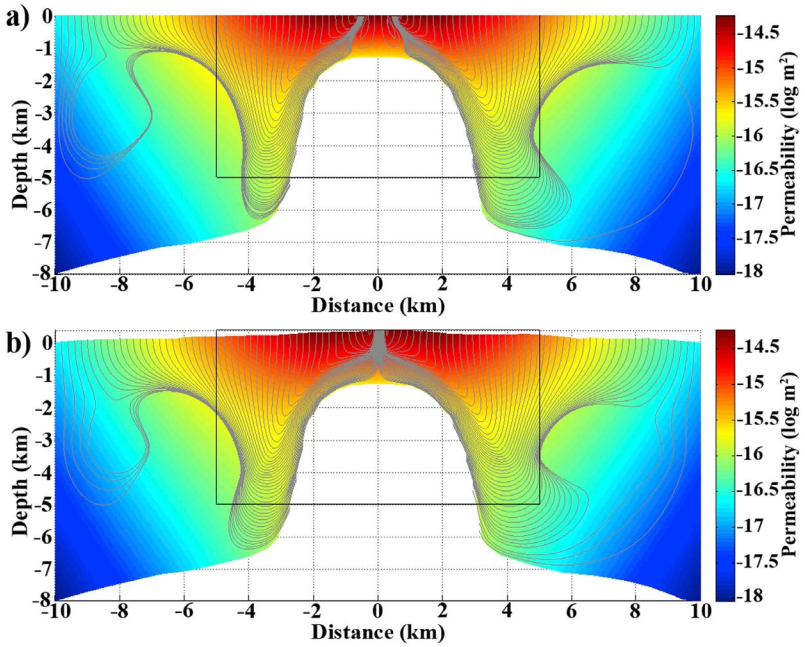

Figure 6. Permeability structures used in the simulations of East Pacific Rise 9°30′N. The permeability decreases both with depth and the distance from the ridge axis. The black boxes in the figures are the domains plotted in Figure 7. (a) The permeability structure and late stage flow lines for the flat top simulation and (b) for the simulation with bathymetric relief. Note how the flow lines visualize pervasive off-axis hydrothermal flow.

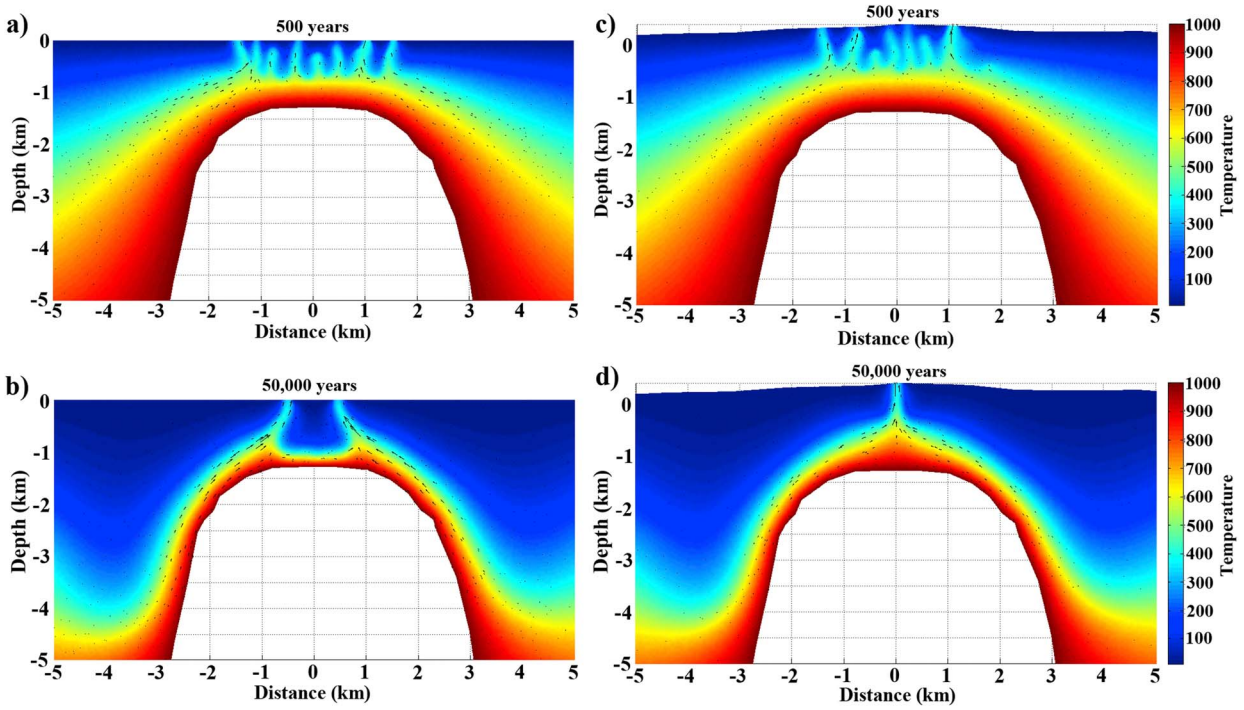

Figure 7. Simulation results (2-D temperature profiles) for the hydrothermal vent field at East Pacific Rise 9°30′N. A hot crust slot is buried 1600 m below the seafloor. (a and c) The early stages of simulations with and without bathymetric relief, respectively. (b and d) The late stage of the simulations. Venting exclusively focuses onto the ridge axis only if bathymetric effects on hydrothermal flow are accounted for. The figures are restricted to dimensions of 5 × 5 km to focus on the vent-site.

locations (Figure 6a). This is due to the fact that upwelling hydrothermal fluids along the margins of the magma chamber are not efficiently focused onto the axis and that several convection cells develop directly above the hot crust (Figure 7). This simulation is therefore inconsistent with the existing observations that all venting occurs directly on-axis.

[28] In contrast, the simulation with bathymetric relief predicts exclusive on-axis venting (Figures 7b and 7d). The plumes forming above the hot crust and the upwelling along the magma chamber coalesce to form fewer plumes which lean toward the axial high ultimately forming a central plume that vents directly on-axis. This clearly shows the effect of bathymetry to form and focus the central plume at the axial high, even though the bathymetric relief is quite smooth. Off-axis venting is suppressed due to the assumption that permeability decreases with increasing distance to the ridge axis, which is consistent with the current observations at EPR. However, it should be noted that detailed off-axis surveys have not been conducted at EPR and may, in future, provide new constraints on vent-locations farther away from the ridge axis. This would require a reassessment of the overall flow pattern but will not change the outcome of this study showing the influence of bathymetry on on-axis vent-locations.

4.2. Lucky Strike Vent Field

4.2.1. Geological Setting

[29] Lucky strike is one of the largest hydrothermal fields located on the slow spreading Mid-Atlantic Ridge (MAR) with 21 active chimney sites at approximately 1740 m depth [http://www.interridge.org/irvents/content/lucky-strike]. The full spreading rate at Lucky-Strike vent field is ~21 mm/yr [*Dziak et al.*, 2004]. The field is located at 37°17′29″N, 32°16′4″W, 400 km southwest of the Azores islands and is part of a group of four main hydrothermal vent fields (Menez Gwenn, Lucky Strike, Saldanha and Rainbow). The presence of a bathymetric high and a hydrothermal field surrounding a central lava lake led to the suggestion of a shallow axial magma chamber [*Fouquet et al.*, 1995]. Furthermore, recent data from reflection seismic, which surveyed the Lucky Strike confirmed this hypothesis [*Singh et al.*, 2006]. An AMC was discovered around 3 km beneath the Lucky Strike volcano which spreads about 7 km along the strike of the ridge with a width of 3–4 km [*Singh et al.*, 2006].

4.2.2. Model Setup

[30] In order to simulate hydrothermal convection at the Lucky Strike vent field, a depth-converted seismic section across the ridge axis was digitized and meshed [*Dusunur et al.*, 2009]. The length of the seismic line is ~16 km and the magma chamber is buried ~3 km below the seafloor. The depth of the modeled domain is 6 km and the depth of the seafloor is 1740 m below sea level. Similar to EPR, the initial temperature and pressure are set to 10°C and hydrostatic values, respectively. The 1000°C AMC with a maximum width of 8400 m at the bottom of model is responsible for driving hydrothermal convection. The permeability structure is unknown at the Lucky Strike vent field, but most likely influenced by bounding faults and fracture network. We nevertheless use a similar permeability model as in the preceding case study for the EPR

$$k = 2 \times 10^{-15} \times \exp\left(-3.6 \times 10^{-3} T\right) \quad (9)$$

$$k^* = k \times \exp\left(-6 \times 10^{-4} x\right) \quad (10)$$

where x is the absolute distance from 1500 m away from the ridge axis. The temperature in equation (9) is again the hypothetical steady state conductive temperature for the given boundary conditions and the magma chamber is assumed to be impermeable. The surface permeability of the Lucky Strike vent field at the spreading center is assumed to be $\sim 2 \times 10^{-15} m^2$, which is lower than in the EPR case study. This is assumed to account for the idea that the crustal permeability at slow spreading ridges is generally lower than at their faster counterparts [*Fouquet*, 1997]. Figure 8 illustrates the permeability structure for the simulations of Lucky Strike. Strictly speaking, the Lucky Strike vent field is situated below the critical end point of water so that boiling and condensation effects could be important. Two-phase phenomena cannot be accurately resolved in the here employed single-phase model and are neglected. Two simulations, i.e., flat surface and real bathymetric relief were performed. The number of elements in these simulations is approximately 1000 per square kilometer.

4.2.3. Results

[31] Convection initiates by the formation of several small plumes at the top of the magma chamber in the simulations with and without bathymetric relief (Figures 9a and 9c). Note that similar to EPR, the figure dimensions for presented results are

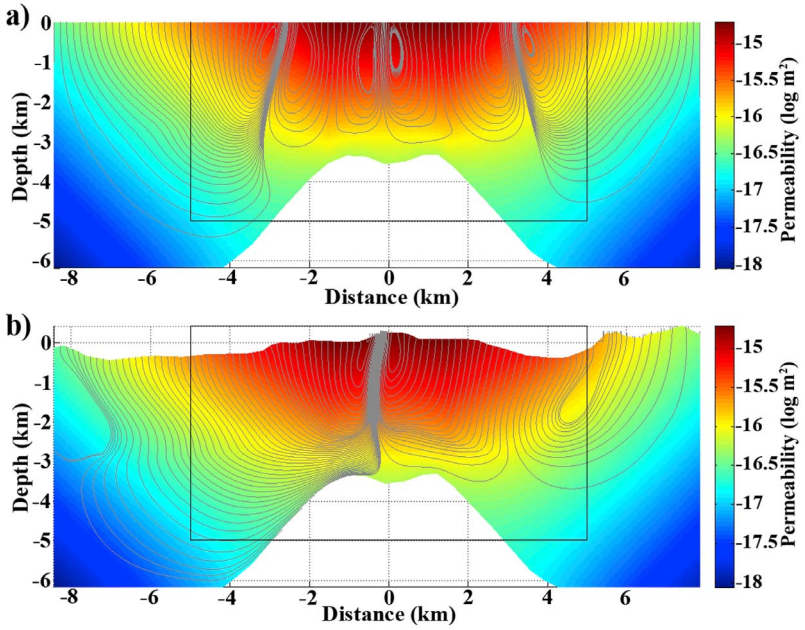

Figure 8. Permeability structure defined for Lucky-Strike vent field. The permeability decreases both with depth and the distance from the ridge axis. The black boxes in the figures are the domains plotted in Figure 9. (a) The permeability structure and late stage flow lines for the flat top simulation and (b) for the simulation with bathymetric relief.

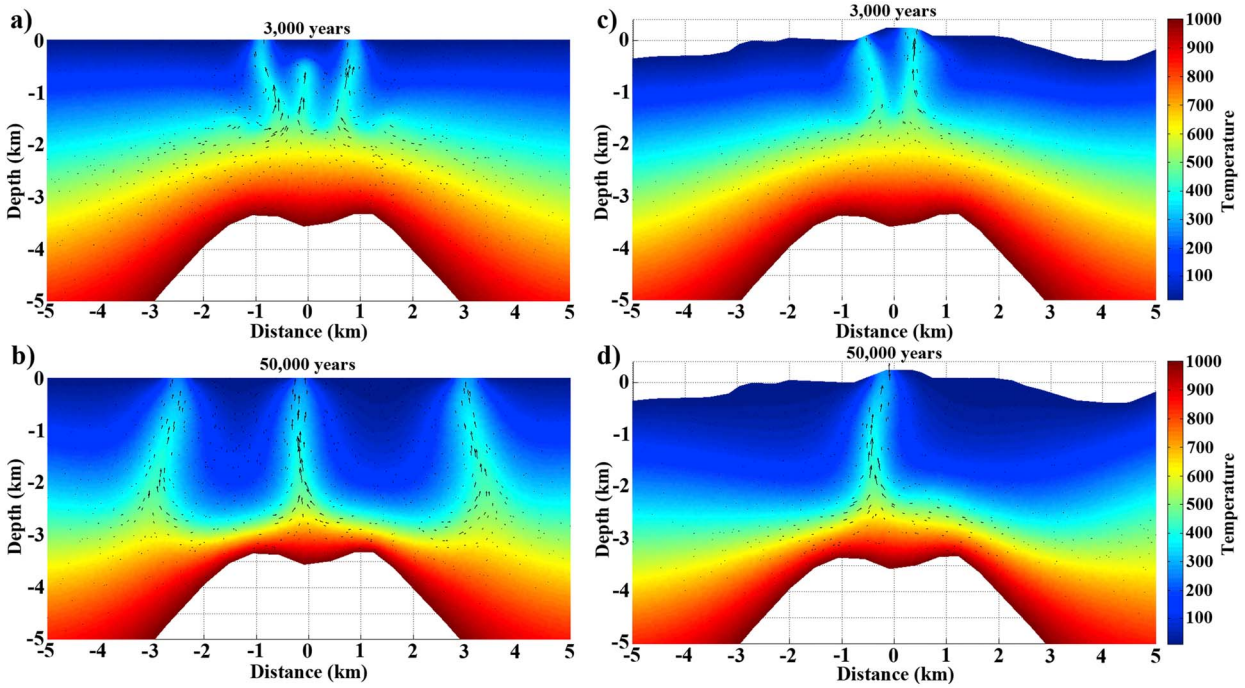

Figure 9. Two-dimensional cross-section of modeled temperature field for the Lucky Strike vent field at (a and c) early and (b and d) late stages. The simulations show that in presence of topography, plumes always vent at local highs, whereas in the flat-surface simulation, plumes may vent off-axis. The late stage of the topographic model shows that vent field is located along the axis of the ridge (Figures 9b and 9d). The figures are limited to 5 × 5 km to show the vent-site more clearly.

limited to 5 × 5 km to demonstrate the vent-site more clearly. In the flat surface scheme, two plumes vent at the top of magma chamber after 3000 years of convection (Figure 9a). Multiple plumes are later formed which merge with previously formed plumes and cause interference resulting in the lateral movement of the vent sites at the surface. The system reaches a quasi-steady state where three plumes are present after 50,000 years of convection (Figure 9b). Note that far off-axis venting does not appear as the temperature gradient as well as the matrix permeability is not high enough to allow convection. The flow patterns show that relatively large convection cells appear above the magma chamber (Figure 8a). Similar to the EPR case study, the simulation that neglects bathymetric effects never predicts exclusive venting at the central volcano and is therefore inconsistent with observations. Only when the effects of bathymetric relief are included, the plumes coalesce to form a single upwelling zone below the vent field on top of the central volcano. Plumes initiating away from the central vent field (Figure 9d) will also merge with this central plume and system reaches a steady state. The simulations confirm that bathymetric relief can also have strong controls on vent site location at slow spreading ridges. Here we have only looked at the special case of the Lucky Strike segment, which shows an on-axis melt lens. Due the significant bathymetric relief of slow-spreading ridges, on- as well as off-axis venting at different ridge segments may well be strongly controlled by bathymetry – in addition to detachment faulting, fracturing and phase separation in multicomponent fluids.

5. Conclusions

[32] We have explored the effects of bathymetric relief on hydrothermal convection in a series of synthetic numerical experiments and two case studies. The presented hydrothermal convection models with unstructured meshes allow us to resolve the effects of bathymetric relief. Venting tends towards bathymetric highs as a result of bathymetry and temperature induced pressure variations in submarine hydrothermal systems. Simulations using a single plume and bathymetric high allow us to predict the maximum deviation from vertical plume ascent as a function of seafloor relief as well as the depth to the heat source. The surface slope in simulations with multiple plumes and highs controls how efficiently venting is focused on the bathymetric highs.

[33] At fast spreading ridges, the axial high helps to focus venting directly onto the ridge axis. Pervasive and deeply penetrating across-axis flow, which is thought to shape the hot crust at fast-spreading ridges, can be reconciled with on-axis venting if bathymetric effects are accounted for. The Lucky Strike case study shows that also on slow-spreading ridges bathymetric relief results in focusing of hydrothermal venting at bathymetric highs – at least for systems in a magmatic phase with an axial magma chamber. Our findings demonstrate the importance of including bathymetry in simulations of submarine hydrothermal flow. In addition to the here presented results on oceanic spreading centers, bathymetric effects should also be important for other submarine vent systems like caldera structures and seamounts.

Acknowledgments

[34] The authors would like to thank the anonymous reviewers for the constructive comments and criticisms which greatly improved the manuscript. N. Bani-Hassan, K. Iyer and L. H. Rüpke are part of the Future Ocean - Excellence Cluster at Kiel. A. Borgia acknowledges support by the American Recovery and Reinvestment Act (ARRA), through the Assistant Secretary for Energy Efficiency and Renewable Energy (EERE), Office of Technology Development, Geothermal Technologies Program, of the U.S. Department of Energy under contract DE-AC02-05CH11231.

References

Allen, D. E., and W. E. Seyfried (2003), Compositional controls on vent fluids from ultramatic-hosted hydrothermal systems at mid-ocean ridges: An experimental study at 400°C, 500 bars, *Geochim. Cosmochim. Acta*, *67*(8), 1531–1542, doi:10.1016/S0016-7037(02)01173-0.

Bach, W., C. J. Garrido, H. Paulick, J. Harvey, and M. Rosner (2004), Seawater-peridotite interactions: First insights from ODP Leg 209, MAR 15°N, *Geochem. Geophys. Geosyst.*, *5*, Q09F26, doi:10.1029/2004GC000744.

Baker, E. T., and C. R. German (2004), On the global distribution of hydrothermal vent fields, in *Mid-Ocean Ridges: Hydrothermal Interactions Between the Lithosphere and Oceans*, *Geophys. Monogr. Ser.*, vol. 148, edited by C. R. German, J. Lin, and L. M. Parson, pp. 245–266, AGU, Washington, D. C., doi:10.1029/148GM10.

Baran, J. M., J. R. Cochran, S. M. Carbotte, and M. R. Nedimovic (2005), Variations in upper crustal structure due to variable mantle temperature along the Southeast Indian Ridge, *Geochem. Geophys. Geosyst.*, *6*, Q11002, doi:10.1029/2005GC000943.

Bauer, O. (1998), PROST: Properties of Water and Steam, software, Hamburg Univ. of Technol., Hamburg, Germany.

Boetius, A. (2005), Lost city life, *Science*, *307*(5714), 1420–1422, doi:10.1126/science.1109849.

Carbotte, S. M., and K. C. Macdonald (1994), The axial topographic high at intermediate and fast spreading ridges,

Earth Planet. Sci. Lett., *128*(3–4), 85–97, doi:10.1016/0012-821X(94)90137-6.

Cathles, L. M., A. H. J. Erendi, and T. Barrie (1997), How long can a hydrothermal system be sustained by a single intrusive event?, *Econ. Geol.*, *92*(7–8), 766–771, doi:10.2113/gsecongeo.92.7-8.766.

Charlou, J. L., J. P. Donval, P. Jean-Baptiste, and A. Dapoigny (1996), Gases and helium isotopes in high temperature solutions sampled before and after ODP Leg 158 drilling at TAG hydrothermal field (26°N, MAR), *Geophys. Res. Lett.*, *23*(23), 3491–3494, doi:10.1029/96GL02141.

Charlou, J. L., J. P. Donval, Y. Fouquet, P. Jean-Baptiste, and N. Holm (2002), Geochemistry of high H_2 and CH_4 vent fluids issuing from ultramafic rocks at the Rainbow hydrothermal field (36°14′N, MAR), *Chem. Geol.*, *191*(4), 345–359, doi:10.1016/S0009-2541(02)00134-1.

Cherkaoui, A. S. M., and W. S. D. Wilcock (1999), Characteristics of high Rayleigh number two-dimensional convection in an open-top porous layer heated from below, *J. Fluid Mech.*, *394*, 241–260, doi:10.1017/S0022112099005716.

Cherkaoui, A. S. M., W. S. D. Wilcock, R. A. Dunn, and D. R. Toomey (2003), A numerical model of hydrothermal cooling and crustal accretion at a fast spreading mid-ocean ridge, *Geochem. Geophys. Geosyst.*, *4*(9), 8616, doi:10.1029/2001GC000215.

Coakley, B. J., and J. R. Cochran (1998), Gravity evidence of very thin crust at the Gakkel Ridge (Arctic Ocean), *Earth Planet. Sci. Lett.*, *162*(1–4), 81–95, doi:10.1016/S0012-821X(98)00158-7.

Coumou, D., T. Driesner, S. Geiger, C. A. Heinrich, and S. Matthäi (2006), The dynamics of mid-ocean ridge hydrothermal systems: Splitting plumes and fluctuating vent temperatures, *Earth Planet. Sci. Lett.*, *245*(1–2), 218–231, doi:10.1016/j.epsl.2006.02.044.

Coumou, D., T. Driesner, and C. A. Heinrich (2008), The structure and dynamics of mid-ocean ridge hydrothermal systems, *Science*, *321*(5897), 1825–1828, doi:10.1126/science.1159582.

Coumou, D., T. Driesner, P. Weis, and C. A. Heinrich (2009a), Phase separation, brine formation, and salinity variation at Black Smoker hydrothermal systems, *J. Geophys. Res.*, *114*, B03212, doi:10.1029/2008JB005764.

Coumou, D., T. Driesner, S. Geiger, A. Paluszny, and C. A. Heinrich (2009b), High-resolution three-dimensional simulations of mid-ocean ridge hydrothermal systems, *J. Geophys. Res.*, *114*, B07104, doi:10.1029/2008JB006121.

Dabrowski, M., M. Krotkiewski, and D. W. Schmid (2008), MILAMIN: MATLAB-based finite element method solver for large problems, *Geochem. Geophys. Geosyst.*, *9*, Q04030, doi:10.1029/2007GC001719.

deMartin, B. J., R. A. R. Canales, J. P. Canales, and S. E. Humphris (2007), Kinematics and geometry of active detachment faulting beneath the Trans-Atlantic Geotraverse (TAG) hydrothermal field on the Mid-Atlantic Ridge, *Geology*, *35*(8), 711–714, doi:10.1130/G23718A.1.

Detrick, R. S., P. Buhl, E. Vera, J. Mutter, J. Orcutt, J. Madsen, and T. Brocher (1987), Multichannel seismic imaging of a crustal magma chamber along the East Pacific Rise, *Nature*, *326*(6108), 35–41, doi:10.1038/326035a0.

Dick, H. J. B., J. Lin, and H. Schouten (2003), An ultraslow-spreading class of ocean ridge, *Nature*, *426*(6965), 405–412, doi:10.1038/nature02128.

Dunn, R. A., D. R. Toomey, and S. C. Solomon (2000), Three-dimensional seismic structure and physical properties of the crust and shallow mantle beneath the East Pacific Rise at 9°30′N, *J. Geophys. Res.*, *105*(B10), 23,537–23,555, doi:10.1029/2000JB900210.

Dusunur, D., J. Escartín, V. Combier, T. Seher, W. Crawford, M. Cannat, S. C. Singh, L. M. Matias, and J. M. Miranda (2009), Seismological constraints on the thermal structure along the Lucky Strike segment (Mid-Atlantic Ridge) and interaction of tectonic and magmatic processes around the magma chamber, *Mar. Geophys. Res.*, *30*(2), 105–120, doi:10.1007/s11001-009-9071-3.

Dziak, R. P., D. K. Smith, D. R. Bohnenstiehl, C. G. Fox, D. Desbruyeres, H. Matsumoto, M. Tolstoy, and D. J. Fornari (2004), Evidence of a recent magma dike intrusion at the slow spreading Lucky Strike segment, Mid-Atlantic Ridge, *J. Geophys. Res.*, *109*, B12102, doi:10.1029/2004JB003141.

Escartín, J., D. K. Smith, J. Cann, H. Schouten, C. H. Langmuir, and S. Escrig (2008), Central role of detachment faults in accretion of slow-spreading oceanic lithosphere, *Nature*, *455*(7214), 790–794, doi:10.1038/nature07333.

Fisher, A. T. (2003), Geophysical constraints on hydrothermal circulation, in *Dahlem Workshop Report, Energy and Mass Transfer in Marine Hydrothermal Systems*, edited by P. E. Halbach, V. Tunnicliffe and J. R. Hein, pp. 29–52, Dahlem Univ. Press, Berlin.

Fisher, A. T., K. Becker, T. N. Narasimhan, M. G. Langseth, and M. J. Mottl (1990), Passive, off-axis convection through the southern flank of the Costa Rica Rift, *J. Geophys. Res.*, *95*(B6), 9343–9370, doi:10.1029/JB095iB06p09343.

Fisher, A. T., K. Becker, and T. N. Narasimhan (1994), Off-axis hydrothermal circulation: Parametric tests of a refined model of processes at Deep Sea Drilling Project/Ocean Drilling Program site 504, *J. Geophys. Res.*, *99*(B2), 3097–3121, doi:10.1029/93JB02741.

Fontaine, F. J., and W. S. D. Wilcock (2007), Two-dimensional numerical models of open-top hydrothermal convection at high Rayleigh and Nusselt numbers: Implications for mid-ocean ridge hydrothermal circulation, *Geochem. Geophys. Geosyst.*, *8*, Q07010, doi:10.1029/2007GC001601.

Foulger, G. R. (2010), *Plates vs. Plumes: A Geological Controversy*, John Wiley, Chichester, U. K., doi:10.1002/9781444324860.

Fouquet, Y. (1997), Where are the large hydrothermal sulphide deposits in the oceans?, *Philos. Trans. R. Soc. London, Ser. B*, *355*, 427–441, doi:10.1098/rsta.1997.0015.

Fouquet, Y., H. Ondreas, J. L. Charlou, J. P. Donval, J. Radfordknoery, I. Costa, N. Lourenco, and M. K. Tivey (1995), Atlantic lava lakes and hot vents, *Nature*, *377*(6546), 201, doi:10.1038/377201a0.

Garg, S. K., and J. W. Pritchett (1977), On pressure-work, viscous dissipation and the energy balance relation for geothermal reservoirs, *Adv. Water Resour.*, *1*(1), 41–47, doi:10.1016/0309-1708(77)90007-0.

Geiger, S., S. Robert, S. K. Matthai, C. Zoppou, and A. Burri (2004), Combining finite element and finite volume methods for efficient multiphase flow simulations in highly heterogeneous and structurally complex geologic media, *Geofluids*, *4*(4), 284–299, doi:10.1111/j.1468-8123.2004.00093.x.

Hartline, B. K., and C. R. B. Lister (1981), Topographic forcing of supercritical convection in a porous-medium such as the oceanic-crust, *Earth Planet. Sci. Lett.*, *55*(1), 75–86, doi:10.1016/0012-821X(81)90088-1.

Haymon, R. M., R. A. Koski, and M. J. Abrams (1989), Hydrothermal discharge zones beneath massive sulfide deposits mapped in the Oman ophiolite, *Geology*, *17*(6), 531–535, doi:10.1130/0091-7613(1989)017<0531:HDZBMS>2.3.CO;2.

Haymon, R. M., D. J. Fornari, M. H. Edwards, S. M. Carbotte, D. Wright, and K. C. Macdonald (1991), Hydrothermal vent distribution along the East Pacific Rise crest (9°09′–54′N) and its relationship to magmatic and tectonic processes on fast-spreading mid-ocean ridges, *Earth Planet. Sci. Lett.*, *104*(2–4), 513–534, doi:10.1016/0012-821X(91)90226-8.

Ingebritsen, S. E., W. E. Sanford, and C. E. Neuzil (2006), *Groundwater Flow in Geologic Processes*, 2nd ed., Cambridge Univ. Press, Cambridge, U. K.

Iyer, K., H. Austrheim, T. John, and B. Jamtveit (2008), Serpentinization of the oceanic lithosphere and some geochemical consequences: Constraints from the Leka Ophiolite Complex, Norway, *Chem. Geol.*, *249*(1–2), 66–90, doi:10.1016/j.chemgeo.2007.12.005.

Iyer, K., L. H. Rupke, and J. P. Morgan (2010), Feedbacks between mantle hydration and hydrothermal convection at ocean spreading centers, *Earth Planet. Sci. Lett.*, *296*(1–2), 34–44, doi:10.1016/j.epsl.2010.04.037.

Kawada, Y., N. Seama, and T. Urabe (2011), The role of seamounts in the transport of heat and fluids: Relations among seamount size, circulation patterns, and crustal heat flow, *Earth Planet. Sci. Lett.*, *306*(1–2), 55–65, doi:10.1016/j.epsl.2011.03.029.

Kelley, D. S., et al. (2005), A serpentinite-hosted ecosystem: The lost city hydrothermal field, *Science*, *307*(5714), 1428–1434, doi:10.1126/science.1102556.

Kent, G. M., A. J. Harding, and J. A. Orcutt (1993), Distribution of magma beneath the East Pacific Rise between the Clipperton Transform and the 9°17N Deval from forward modeling of common depth point data, *J. Geophys. Res.*, *98*(B8), 13,945–13,969, doi:10.1029/93JB00705.

Kleinrock, M. C., B. E. Tucholke, J. Lin, and M. A. Tivey (1997), Fast rift propagation at a slow-spreading ridge, *Geology*, *25*(7), 639–642, doi:10.1130/0091-7613(1997)025<0639:FRPAAS>2.3.CO;2.

Koschinsky, A., D. Garbe-Schonberg, S. Sander, K. Schmidt, H. H. Gennerich, and H. Strauss (2008), Hydrothermal venting at pressure-temperature conditions above the critical point of seawater, 5°S on the Mid-Atlantic Ridge, *Geology*, *36*(8), 615–618, doi:10.1130/G24726A.1.

Lister, C. R. B. (1980), Heat-flow and hydrothermal circulation, *Annu. Rev. Earth Planet. Sci.*, *8*, 95–117, doi:10.1146/annurev.ea.08.050180.000523.

Lowell, R. P. (1980), Topographically driven subcritical hydrothermal convection in the oceanic-crust, *Earth Planet. Sci. Lett.*, *49*(1), 21–28, doi:10.1016/0012-821X(80)90145-4.

Marques, A. F. A., F. Barriga, and S. D. Scott (2007), Sulfide mineralization in an ultramafic-rock hosted seafloor hydrothermal system: From serpentinization to the formation of Cu-Zn-(Co)-rich massive sulfides, *Mar. Geol.*, *245*(1–4), 20–39, doi:10.1016/j.margeo.2007.05.007.

Morgan, J. P., and Y. J. Chen (1993), The genesis of oceanic-crust: Magma injection, hydrothermal circulation, and crustal flow, *J. Geophys. Res.*, *98*(B4), 6283–6297, doi:10.1029/92JB02650.

Murton, B. J., et al. (1994), Direct evidence for the distribution and occurrence of hydrothermal activity between 27°N–30°N on the Mid-Atlantic Ridge, *Earth Planet. Sci. Lett.*, *125*(1–4), 119–128, doi:10.1016/0012-821X(94)90210-0.

Nicolas, A., D. Mainprice, and F. Boudier (2003), High-temperature seawater circulation throughout crust of oceanic ridges: A model derived from the Oman ophiolites, *J. Geophys. Res.*, *108*(B8), 2371, doi:10.1029/2002JB002094.

Schmidt, K., A. Koschinsky, D. Garbe-Schonberg, L. M. de Carvalho, and R. Seifert (2007), Geochemistry of hydrothermal fluids from the ultramafic-hosted Logatchev hydrothermal field, 15°N on the Mid-Atlantic Ridge: Temporal and spatial investigation, *Chem. Geol.*, *242*(1–2), 1–21, doi:10.1016/j.chemgeo.2007.01.023.

Searle, R. C., J. A. Keeton, R. B. Owens, R. S. White, R. Mecklenburgh, B. Parsons, and S. M. Lee (1998), The Reykjanes Ridge: Structure and tectonics of a hot-spot-influenced, slow-spreading ridge, from multibeam bathymetry, gravity and magnetic investigations, *Earth Planet. Sci. Lett.*, *160*(3–4), 463–478, doi:10.1016/S0012-821X(98)00104-6.

Singh, S. C., W. C. Crawford, H. Carton, T. Seher, V. Combier, M. Cannat, J. P. Canales, D. Dusunur, J. Escartín, and J. M. Miranda (2006), Discovery of a magma chamber and faults beneath a Mid-Atlantic Ridge hydrothermal field, *Nature*, *442*(7106), 1029–1032, doi:10.1038/nature05105.

Smith, D. K., and J. R. Cann (1992), The role of seamount volcanism in crustal construction at the Mid-Atlantic Ridge (24°–30°N), *J. Geophys. Res.*, *97*(B2), 1645–1658, doi:10.1029/91JB02507.

Theissen-Krah, S., K. Iyer, L. Rüpke, and J. P. Morgan (2011), Coupled mechanical and hydrothermal modeling of crustal accretion at intermediate to fast spreading ridges, *Earth Planet. Sci. Lett.*, *311*(3–4), 275–286, doi:10.1016/j.epsl.2011.09.018.

Tolstoy, M., D. R. Bohnenstiehl, M. H. Edwards, and G. J. Kurras (2001), Seismic character of volcanic activity at the ultraslow-spreading Gakkel Ridge, *Geology*, *29*(12), 1139–1142, doi:10.1130/0091-7613(2001)029<1139:SCOVAA>2.0.CO;2.

Tolstoy, M., F. Waldhauser, D. R. Bohnenstiehl, R. T. Weekly, and W. Y. Kim (2008), Seismic identification of along-axis hydrothermal flow on the East Pacific Rise, *Nature*, *451*(7175), 181–184, doi:10.1038/nature06424.

Toomey, D. R., S. C. Solomon, and G. M. Purdy (1994), Tomographic imaging of the shallow crustal structure of the East Pacific Rise at 9°30 N, *J. Geophys. Res.*, *99*(B12), 24,135–24,157, doi:10.1029/94JB01942.

Tufar, W., E. Tufar, and J. Lange (1986), Ore paragenesis of recent hydrothermal deposits at the Cocos-Nazca plate boundary (Galapagos Rift) at 85°51′ and 85°55′W: Complex massive sulfide mineralizations, non-sulfidic mineralizations and mineralized basalts, *Geol. Rundsch.*, *75*(3), 829–861, doi:10.1007/BF01820650.

Von Damm, K. L. (1990), Seafloor hydrothermal activity–Black smoker chemistry and chimneys, *Annu. Rev. Earth Planet. Sci.*, *18*, 173–204, doi:10.1146/annurev.ea.18.050190.001133.

Wilcock, W. S. D. (1998), Cellular convection models of mid-ocean ridge hydrothermal circulation and the temperatures of black smoker fluids, *J. Geophys. Res.*, *103*(B2), 2585–2596, doi:10.1029/97JB03252.